SMART-KNEE: Sparse-Morphology based Anatomical Reconstruction using Topology-Aware Networks for Imageless Total Knee Arthroplasty

Durga Rajasekar[1,2*], Swetha Lakshmi S[1,2*], Vishnu M R[2], Vivek Maik[2†], Manojkumar Lakshmanan[2], and Mohanasankar Sivaprakasam[1]

[1] Dept. of Electrical Engineering, Indian Institute of Technology Madras, India
[2] Healthcare Technology Innovation Centre (HTIC), IIT Madras, India
maik.vivek@htic.iitm.ac.in, mohan@ee.iitm.ac.in

Abstract. Imageless Total Knee Arthroplasty (ITKA) requires real-time acquisition of patient-specific anatomical landmarks without preoperative CT or MRI, posing a significant challenge for intraoperative planning. Despite utilising 3D knee reconstruction algorithms, modern ITKA systems continue to struggle with accurate knee shape estimation and the anatomical axis alignment - both prerequisites for reliable ITKA planning. We present SMART-KNEE, a cascaded anatomy-aware reconstruction framework that generates patient-specific Femoral (F) and Tibial(T) bone morphology from a minimal set of intraoperatively collected anatomical landmarks, without preoperative imaging. In the first stage, a Topology-Aware Equivariant Graph Neural Network (EGNN) predicts the complete anatomical landmark set from four intraoperative anchor landmarks, enforcing topological consistency and anatomical plausibility under under E(3)-equivariance (invariance to 3D euclidean transformations). In the second stage, an Anatomy-Aware GAN reconstructs complete patient-specific bone surfaces by fusing the EGNN-predicted landmarks with partial intraoperative surface point clouds. SMART-KNEE achieves precise landmark localization error (F: $2.28\,\mathrm{mm} \pm 1.68\,\mathrm{mm}$; T: $1.65\,\mathrm{mm} \pm 0.83\,\mathrm{mm}$). Test cohort surface reconstruction yields Dice F-87%, T-92.477%, Hausdorff Distance F-5, T-4.3 mm and ground truth - generated knee distances of 1.89 mm (F) and 2.87 mm (T), enabling accurate patient-specific morphology retrieval for intraoperative ITKA planning.Git-Hub

Keywords: Imageless total knee arthroplasty · Topology-aware EGNN · Anatomy-aware GAN · landmark prediction · patient-specific bone reconstruction · intraoperative navigation

1 Introduction

ITKA achieves accurate implant positioning while reducing radiation exposure and cost compared to image-based and conventional systems [17,12,14]. It relies

*Equal contribution
†Corresponding author

on real-time intraoperative data from an optical tracking system, where reference markers on the femur (F) and tibia (T) digitize anatomical landmarks in 3D via a calibrated probe [5], from which a patient-specific knee model is reconstructed to support surgical planning [3,2]. However, sparse landmark-based reconstruction relies on shape assumptions and parametric models [7], often causing inaccurate anatomical axis reconstruction, suboptimal implant sizing, and soft-tissue imbalance [4,3], thereby undermining ITKA relative to imaging-based TKA [10].

Related Works: 3D reconstruction of patient-specific bone morphology from sparse data remains a core challenge in computational orthopaedics. Reconstructing the complete F surface and mechanical axis from sparse landmarks via a Statistical Shape Model (SSM) [8], achieving mechanical axis deviation below 3.5°; however, the fixed low-dimensional shape space limits patient-specific detail. Extended this by morphing SSMs from digitised landmarks for both F and T [13], outperforming linear scaling yet remaining bound to statistical priors. [1] formulated a probabilistic SSM as a Gaussian Mixture Model for surface reconstruction from sparse point clouds, improving robustness, but unable to recover morphological detail beyond the encoded prior. Generative methods using global–local context discriminators have improved region-of-interest fidelity in medical reconstruction [11], motivating context-aware anatomical conditioning. In parallel, E(3)-equivariant graph neural networks have demonstrated substantially improved performance over standard GNNs for 3D biological structure tasks by preserving geometric consistency under arbitrary rotations and translations [15,16]. Existing methods remain constrained by population subspaces and preoperative imaging, leaving a clear gap for a unified imageless framework capable of joint landmark completion and full knee surface reconstruction from sparse intraoperative data.

Contributions: We present SMART-KNEE, a framework combining a Topology-Aware EGNN and an Anatomy-Aware GAN [9] to reconstruct patient-specific F and T morphology from sparse intraoperative data, achieving clinically acceptable accuracy within 3 mm [19]. We further release a publicly available dataset of 361 annotated F and T models with anatomical landmarks and critical distal and proximal surface regions.

2 Methodology

Dataset: The dataset comprises patient-specific F and T bone models from a publicly available repository [6], each annotated with 12 F and 11 T landmarks (Table 1), of which 4 anchors per bone serve as known intraoperative inputs, and the remainder are predicted by the EGNN. Beyond the joint-line ROI, the predicted landmark set includes the hip centre (FHC) and ankle centre (AC), enabling mechanical-axis alignment computation, a core requirement for TKA planning. Sparse point clouds sampled from the F anterior cortex, distal and posterior condyles, and proximal T plateaus and tuberosity simulate intraoperative probe acquisition, and together with the predicted landmarks from the two conditioning inputs to the Anatomy-Aware GAN (Fig. 1).

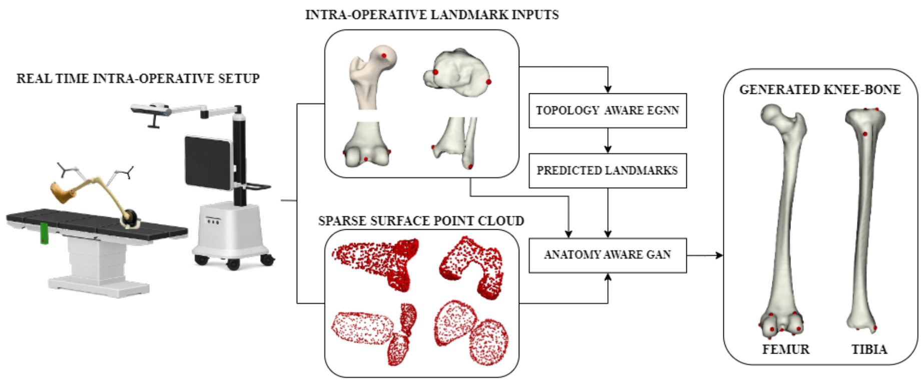

Fig. 1: SMART-KNEE framework: Intraoperative anchor landmarks are processed by the Topology-Aware EGNN to complete the landmark set, which the Anatomy-Aware GAN fuses with the partial point cloud to reconstruct complete patient-specific F and T bone surfaces for ITKA planning.

Table 1: Anatomical landmarks annotated per bone in the SMART-KNEE dataset.(F – Femur, T – Tibia, Med. – Medial, Lat. – Lateral, Ant. – Anterior, Post. – Posterior, Cond. – Condyle, Prox. – Proximal, Lig. – Ligament.)

Femur		
ID	**Acro.**	**Landmark**
0	FHC	Hip Center
1	FKC	Knee Center
2	FME	Medial Epicondyle
3	FLE	Lateral Epicondyle
4	FMDC	Medial Distal Condyle
5	FLDC	Lateral Distal Condyle
6	FMPC	Medial Post. Condyle
7	FLPC	Lateral Post. Condyle
8	FMAC	Medial Ant. Cortex
9	FLAC	Lateral Ant. Cortex
10	FMCPP	Med. Cond. Prox. Post.
11	FLCPP	Lat. Cond. Prox. Post.

Tibia		
ID	**Acro.**	**Landmark**
0	TKC	Knee Center
1	TMP	Medial Plateau
2	TLP	Lateral Plateau
3	TMC	Medial Condyle
4	TLC	Lateral Condyle
5	TT	Tuberosity
6	TPCL	Post. Cruciate Lig.
7	TACL	Ant. Cruciate Lig.
8	MM	Medial Malleolus
9	LM	Lateral Malleolus
10	AC	Ankle Center

Topology-Aware EGNN-based Landmark Completion: Knee anatomy is modelled as a graph where landmarks are nodes and spatial interactions are edges, partitioned into $K = 4$ known anchors and $|\mathcal{U}| = N - K$ unknown targets-8 F and 7 T. The Kabsch–Umeyama transform aligns the mean canonical shape to the known anchors, providing anatomically plausible initial coordinates [18]. Each node encodes its known/unknown status, knee chirality, and geometric descriptors; over $L = 4$ equivariant message-passing layers, landmarks itera-

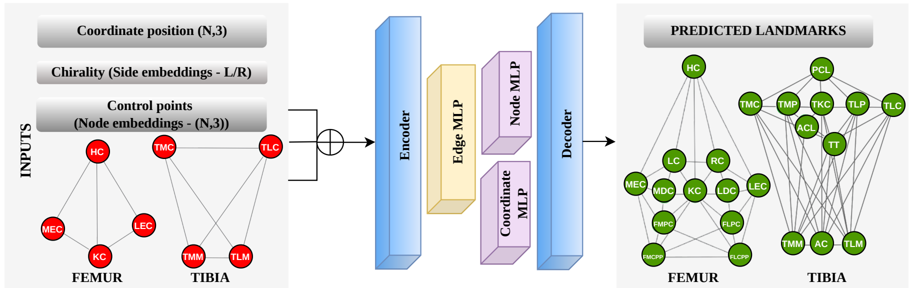

Fig. 2: Topology-Aware EGNN for intraoperative landmark prediction, mapping sparse known anchor nodes (red) from F and T graphs to a complete set of predicted anatomical landmarks (green) via equivariant message passing over geometric and chirality-conditioned node embeddings.

Algorithm 1 Topology-Aware EGNN for Landmark Completion

Require: $A_{m\times n}$ (Initial Positions), b_m (Target Positions), $\bar{n}_p$ (Mean Shape Template), $\mathcal{E}$ (Graph Edges), $w_{\text{position}}, w_{\text{edge}}$ (Loss Weights)
Ensure: Predicted coordinates n_i^{final}, nodes weights x_w
  Initialisation: $n_i^{(0)} \leftarrow s^* R^* \bar{n}_p + t^*$ via Kabsch–Umeyama
  Node Encoding: $h_i^{(0)} \leftarrow \text{MLP}_{\text{enc}}(e_{\text{side}} \oplus e_{\text{known}} \oplus n_i^{(0)} \oplus g_i)$
  for $l = 0$ to $L-1$ **do**
    $m_{ij}^{(l)} = \text{MLP}_{\text{edge}}(h_i^{(l)}, h_j^{(l)}, \|n_i^{(l)} - n_j^{(l)}\|^2)$
    $h_i^{(l+1)} = \text{MLP}_{\text{node}}(h_i^{(l)}, \sum m_{ij}^{(l)})$
  end for
  Decoding: $n_i^{\text{final}} \leftarrow n_i^{(0)} + \text{clip}(\text{MLP}_{\text{dec}}(h_i^{(L)}), -0.5, 0.5) + \bar{c}_k$
  Loss: $\mathcal{L} = w_{\text{pos}} \sum \|n_i^{\text{final}} - n_i^{\text{target}}\|_1 + w_{\text{edge}} \sum \big| \|n_i^{\text{final}} - n_j^{\text{final}}\|_2 - d_{ij}^{\text{target}} \big|$
  if $A_{ij} x_w = b_{j_{\min}}$ **then** $x_w \leftarrow I$
  else $x_w \leftarrow (A_{ij}^T A_{ij})^{-1} A_{ij}^T b_{j_{\min}}$
  end if

---

tively refine both feature states and 3D positions via learnt gated aggregation. A decoder MLP then applies a clipped coordinate correction, denormalized to millimetre space. Training minimises a composite loss penalising positional error, inter-landmark distance deviation, and ensuring anatomical fidelity across all predicted landmarks (Fig.2) (Algorithm 1).

Anatomy-Aware GAN-based Bone Surface Reconstruction: The framework reconstructs complete 3D knee surfaces from partial intraoperative point clouds conditioned on EGNN-predicted landmarks, trained in two phases: autoencoder training followed by conditional adversarial training (Algorithm 2).
A PointNet autoencoder is trained on complete knee surfaces to establish a structured latent geometry manifold (Fig. 3), optimised via the symmetric Chamfer Distance $\mathcal{L}_{\text{CD}}$. Once trained, all weights are frozen and reused in Phase 2. The generator encodes the patch encoder, and a landmark encoder captures local

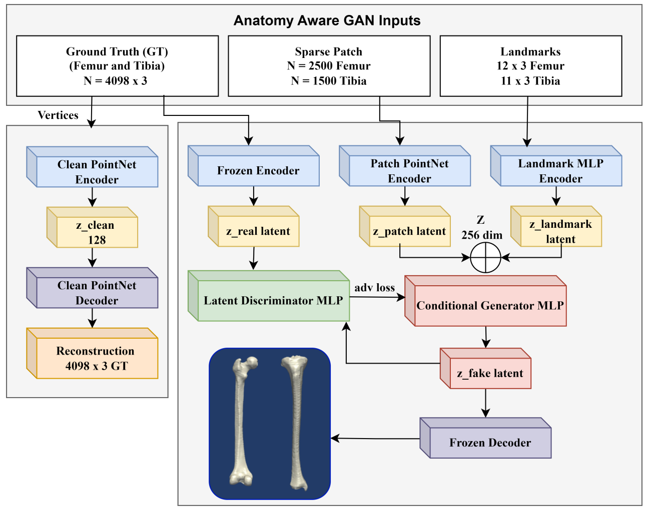

Fig. 3: Anatomy-Aware GAN architecture for patient-specific knee (F&T) surface reconstruction.

surface topology and patient-specific proportions, respectively. It fuses both into a single latent code z_{gen}, rendered into a complete point cloud by the Frozen Decoder, supervised jointly by adversarial realism $\mathcal{L}_{G_{\text{adv}}}$, patch surface coverage $\mathcal{L}_{\text{Patch}}$, and landmark fidelity $\mathcal{L}_{\text{Lmk}}$ losses.

Algorithm 2 Anatomy-Aware GAN for 3D Bone Surface Reconstruction

Require: P (partial surface), S (complete bone), L (landmarks), $d = 128$, $N = 4096$
Ensure: Watertight mesh $\mathcal{M}$

Phase 1: $z_{\text{clean}} \leftarrow \text{PointNetEnc}(S)$; $\hat{S} \leftarrow \text{PointNetDec}(z_{\text{clean}})$; freeze weights after minimising:

$$\mathcal{L}_{\text{CD}}(S, \hat{S}) = \frac{1}{|S|} \sum_{x \in S} \min_{y \in \hat{S}} \|x - y\|_2 + \frac{1}{|\hat{S}|} \sum_{y \in \hat{S}} \min_{x \in S} \|x - y\|_2$$

Phase 2: $z_{\text{gen}} \leftarrow \text{Gen}([\text{PatchEnc}(P) \| \text{LmkEnc}(L)])$; $\hat{S}_{\text{gen}} \leftarrow \text{FrozenDec}(z_{\text{gen}})$

$$\mathcal{L}_D = \tfrac{1}{2}\mathbb{E}[(D(z_{\text{clean}}) - 1)^2] + \tfrac{1}{2}\mathbb{E}[(D(z_{\text{gen}}))^2]$$

$$\mathcal{L}_{\text{Total}} = \alpha\,\mathcal{L}_{G_{\text{adv}}} + \beta \max_{p \in P} \min_{q \in \hat{S}_{\text{gen}}} \|p - q\|_2 + \gamma \frac{1}{N_L} \sum_{l \in L} \min_{q \in \hat{S}_{\text{gen}}} \|l - q\|_2^2$$

Phase 3: $\hat{S}_{\text{patient}} \leftarrow (\hat{S}_{\text{gen}} \cdot \mathbf{V}^\top) \cdot \text{scale} + \text{centroid}$; Poisson $\to \mathcal{M}$
if left-sided **then** $\hat{S}_{\text{patient}} \leftarrow \hat{S}_{\text{patient}} \cdot \text{diag}(-1, 1, 1)$
end if

The discriminator utilizes a lightweight MLP to discriminate in the latent space between the frozen encoder's ground-truth code z_{clean} and the generator's code z_{gen} under the LS-GAN objective, driving the generator onto the pretrained geometry manifold. At inference, the output point cloud is unscaled to millimetre space and converted to a watertight mesh via Poisson surface reconstruction.

3 Results and Discussion

The dataset of 361 annotated F and T pairs was divided into 70% training, 15% validation, and 15% testing, with stratified splits to ensure balanced representation of left- and right-sided bones. The 4 known anchor points for each bone were provided intraoperatively, whereas the remaining 8 unknown landmarks for the F and 7 for the T were predicted. Performance was assessed by measuring the per-node landmark Euclidean distance (mm) between predicted and ground-truth coordinates for all unknown nodes.

Table 2: Per-node landmark localisation error (mm, mean) comparing SMART-KNEE against VN-EGNN [16] and E(3) [15]. Nodes 0–3 (Femur) and 3, 4, 9, 10 (Tibia) are known anchors (error = 0).

Femur				**Tibia**			
ID	**VN-EGNN**	**E(3)**	**Ours**	**ID**	**VN-EGNN**	**E(3)**	**Ours**
0	0.00	0.00	0.00	0	8.37	12.72	**2.01**
1	0.00	0.00	0.00	1	8.00	12.29	**1.15**
2	0.00	0.00	0.00	2	8.37	12.47	**1.62**
3	0.00	0.00	0.00	3	0.00	0.00	0.00
4	6.88	9.29	**2.90**	4	0.00	0.00	0.00
5	5.71	9.05	**2.71**	5	6.08	10.16	**1.75**
6	7.60	8.36	**3.06**	6	7.40	11.94	**1.29**
7	7.20	8.45	**2.69**	7	8.37	12.84	**0.45**
8	8.05	7.84	**2.41**	8	8.08	12.39	**3.58**
9	9.71	7.94	**2.76**	9	0.00	0.00	0.00
10	7.22	6.18	**1.61**	10	0.00	0.00	0.00
11	6.75	6.17	**1.45**				
Mean	7.50	7.91	**1.25**	**Mean**	7.81	12.12	**1.69**

The EGNN achieved a mean localisation error of 2.28 ± 1.68 mm for the F and 1.65 ± 0.83 mm for the T. The T yields lower localisation error due to its compact and symmetric proximal geometry, which imposes tighter geometric constraints during equivariant message passing. By contrast, the F's posterior condyle and anterior cortical markers (FMCPP, FLCPP, FMAC, FLAC) lie farther from the four anchor nodes and exhibit greater inter-patient morphological variability. Condylar and plateaus landmarks (FMDC, FLDC, TMP, TLP) consistently achieved errors below 1.5 mm, while proximal-posterior cortex landmarks relied more heavily on global geometric context propagated through the four message-passing layers, with worst-case predictions approaching 3–4 mm.

The flagged anchor geometric diversity drives localisation accuracy: clustering anchors distally (e.g., {3,4,5,6}) yields F errors up to 10.00 mm, while optimal configurations {0,1,2,3} and {3,4,9,10} achieve 2.28±1.68 mm and 1.65±0.83 mm for F and T respectively (4.4× and 4.7× improvements), both within the 3 mm ITKA threshold [19]As shown in Table 2, SMART-KNEE outperforms VN-EGNN [16] and EquiPPIS [15] by up to 6× on F(1.25 ± 0.75 mm vs. 7.50 mm and 7.91 mm) and T(1.69 ± 0.09 mm vs. 7.81 mm and 12.12 mm), with the greatest gains at geometrically remote nodes where topology-aware equivariant message passing most effectively propagates anchor constraints.
The Anatomy-Aware GAN was evaluated on the 39 held-out test subjects by measuring surface reconstruction quality across four standard volumetric and geometric metrics, as illustrated in Fig. 4.

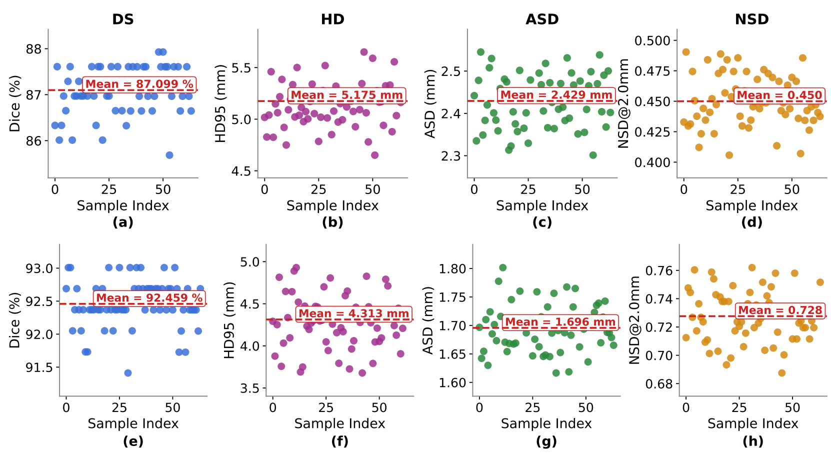

Fig. 4: Assessment of test set using (a,e) Dice Score, (b,f) HD, (c,g) ASD and (d,h) NSD for F (a,b,c,d) and T (e,f,g,h)

The reconstructed bone surfaces achieved a mean Dice score (DS) of F-87%, T-92.477%, Hausdorff Distance (HD95) of F-5.1, T-4.3 mm, Average Surface Distance (ASD) of F-2.4, T-1.6 mm, Normal Surface Distance (NSD) of F-0.45, T-0.7 at a 2.0 mm tolerance, confirming strong volumetric overlap and clinically acceptable surface proximity to ground truth [19]. Per-bone surface distances ground truth to the generated Knee of 2.87 mm for the T and 1.97 mm for the F. reflect the greater morphological complexity of the distal F, particularly the posterior condylar regions, where sparse intraoperative point cloud coverage requires the generator to extrapolate beyond directly sampled geometry.
Maintaining consistent reconstruction quality across diverse morphologies required a dual-conditioning architecture that combined local surface topology from the Patch Encoder with patient-specific anatomical proportions from the Landmark Encoder. Wider articular higher HD95 values, indicating that recon-

struction quality is limited by intraoperative surface acquisition, not generative architecture. The Anatomy-Aware GAN delivers patient-specific bone morphology with adequate geometric fidelity for intraoperative implant planning without preoperative CT or MRI, as the mean ASD of 1.694 mm falls within the accuracy criterion for ITKA [19].

Clinical Evaluation To validate the end-to-end SMART-KNEE pipeline under realistic intraoperative conditions, a clinical evaluation was conducted on a held-out set of subjects. As illustrated in Fig. 5, the integrated system achieved a Landmark RMSE of 0.25 mm and 0.36 mm for the F and T, respectively, confirming that the predicted landmarks align closely with ground-truth positions after registration. The GAN-reconstructed bone surfaces yielded Surface Distances of 0.38 mm (F) and 0.26 mm (T) against the ground-truth CT-derived meshes, demonstrating that the reconstructed morphology faithfully captures true bone geometry.Both metrics fall substantially within the 3 mm ITKA accuracy threshold [19], confirming that the full landmark prediction and surface reconstruction pipeline meets clinical accuracy requirements without preoperative imaging.

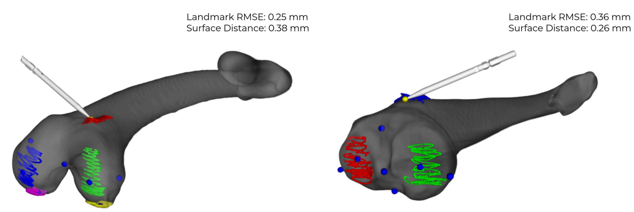

Fig. 5: SMART-KNEE clinical evaluation on a physical phantom: F (left) and T (right) showing predicted landmarks (blue) and acquired surface point clouds (coloured regions) with registration errors.

4 Conclusion

SMART-KNEE presents a two-stage cascaded framework for knee reconstruction in ITKA. A Topology-Aware EGNN first completes the full anatomical landmark set from four sparse intraoperative anchors, where graph-centrality-based anchor selection proves critical to localisation accuracy. An Anatomy-Aware GAN then fuses the predicted landmarks with a sparse surface point cloud to reconstruct complete, patient-specific F and T morphology. All surface errors fall below the clinical threshold for ITKA on both the held-out test cohort and a 3D-printed, CT-derived phantom under optical tracking, demonstrating that the pipeline achieves the geometric accuracy required for imageless implant planning and sizing. These phantom-based results motivate extending validation to cadaveric specimens and real intraoperative, patient-specific TKA settings in future work.

References

1. Bernard, F., Salamanca, L., Thunberg, J., Tack, A., Jentsch, D., Lamecker, H., Zachow, S., Hertel, F., Goncalves, J., Gemmar, P.: Shape-aware surface reconstruction from sparse 3d point-clouds. Medical Image Analysis **38**, 77–89 (May 2017). https://doi.org/10.1016/j.media.2017.02.005
2. Bollars, P., Nathwani, D., Albelooshi, A., Ettinger, M., Verheyden, F., Mievis, J., Meshram, P., Schotanus, M.: Imageless handheld robotic-assisted total knee arthroplasty showed better clinical outcomes than conventional total knee arthroplasty: A randomized controlled trial with preliminary results at 1-year follow up. The Knee **56**, 232–240 (Oct 2025). https://doi.org/10.1016/j.knee.2025.05.028
3. Bosco, F., Rovere, G., Burgio, C., Lo Bue, G., Cobisi, C.D., Giai Via, R., Lucenti, L., Camarda, L.: Accuracy and learning curve of imageless robotic-assisted total knee arthroplasty. Journal of Orthopaedics **66**, 77–83 (Aug 2025). https://doi.org/10.1016/j.jor.2024.12.029
4. Cochrane, N.H., Kim, B.I., Stauffer, T.P., Hallows, R.K., Urish, K.L., Carvajal Alba, J.A., Seyler, T.M.: Revision total knee arthroplasty with an imageless, second-generation robotic system. The Journal of Arthroplasty **39**(8), S280–S284 (Aug 2024). https://doi.org/10.1016/j.arth.2024.02.018
5. Edelstein, A.I., Orsi, A.D., Plaskos, C., Coffey, S., Suleiman, L.I.: Imageless robotic total knee arthroplasty determines similar coronal plane alignment of the knee (cpak) parameters to long leg radiographs. Arthroplasty **6**(1) (Mar 2024). https://doi.org/10.1186/s42836-024-00231-9
6. Fischer, M.C.M.: Database of segmentations and surface models of bones of the entire lower body created from cadaver ct scans. Scientific Data **10**(1) (Nov 2023). https://doi.org/10.1038/s41597-023-02669-z
7. Hirschmann, M.T., Avram, G., Graichen, H., Tandogan, R.N., Mengis, N., Zaffagnini, S.: Same same but different—image-based versus imageless robotic-assisted total knee arthroplasty! Journal of Experimental Orthopaedics **11**(4) (Oct 2024). https://doi.org/10.1002/jeo2.70062
8. Kompella, G., Antico, M., Sasazawa, F., Jeevakala, S., Ram, K., Fontanarosa, D., Pandey, A.K., Sivaprakasam, M.: Segmentation of femoral cartilage from knee ultrasound images using mask r-cnn. In: 2019 41st Annual International Conference of the IEEE Engineering in Medicine and Biology Society (EMBC). IEEE (Jul 2019). https://doi.org/10.1109/embc.2019.8857645, http://dx.doi.org/10.1109/EMBC.2019.8857645
9. Lambrechts, A., Wirix-Speetjens, R., Maes, F., Van Huffel, S.: Artificial intelligence based patient-specific preoperative planning algorithm for total knee arthroplasty. Frontiers in Robotics and AI **9** (Mar 2022). https://doi.org/10.3389/frobt.2022.840282
10. Li, S., Liu, X., Chen, X., Xu, H., Zhang, Y., Qian, W.: Development and validation of an artificial intelligence preoperative planning and patient-specific instrumentation system for total knee arthroplasty. Bioengineering **10**(12), 1417 (Dec 2023). https://doi.org/10.3390/bioengineering10121417
11. Murugesan, B., Vijaya Raghavan, S., Sarveswaran, K., Ram, K., Sivaprakasam, M.: Recon-GLGAN: A Global-Local Context Based Generative Adversarial Network for MRI Reconstruction, p. 3–15. Springer International Publishing (2019). https://doi.org/10.1007/978-3-030-33843-5_1
12. Narkbunnam, R., Chorunchan, Y., Chareancholvanich, K., Achawakulthep, C., Awirotananon, K., Pornrattanamaneewong, C.: Imageless and image-based robotic-

assisted total knee arthroplasty achieve equivalent radiographic accuracy: A randomised controlled trial. Knee Surgery, Sports Traumatology, Arthroscopy (Oct 2025). https://doi.org/10.1002/ksa.70123

13. Nolte, D., Ko, S.T., Bull, A.M., Kedgley, A.E.: Reconstruction of the lower limb bones from digitised anatomical landmarks using statistical shape modelling. Gait & Posture **77**, 269–275 (Mar 2020). https://doi.org/10.1016/j.gaitpost.2020.02.010
14. Rajasekaran, S., Soundarrajan, D., Singh, R., Shiferaw, B.A., Rajasekaran, R.B., Dhanasekararaja, P., Rajkumar, N.: Comparison of imageless robotic assisted total knee arthroplasty and conventional total knee arthroplasty: early clinical and radiological outcomes of 200 knees. Journal of Robotic Surgery **18**(1) (Apr 2024). https://doi.org/10.1007/s11701-024-01905-x
15. Roche, R., Moussad, B., Shuvo, M.H., Bhattacharya, D.: E(3) equivariant graph neural networks for robust and accurate protein-protein interaction site prediction. PLOS Computational Biology **19**(8), e1011435 (Aug 2023). https://doi.org/10.1371/journal.pcbi.1011435
16. Sestak, F., Schneckenreiter, L., Brandstetter, J., Hochreiter, S., Mayr, A., Klambauer, G.: Vn-egnn: E(3)-equivariant graph neural networks with virtual nodes enhance protein binding site identification (2024). https://doi.org/10.48550/ARXIV.2404.07194
17. Tran, J.Y.S., Tang, A.Y.T., Wong, C.K., Lam, G.Y.T., Choi, T.L., Mak, R.W.F., Ng, J.P., Ho, K.K.W., Ong, M.T.Y., Yung, P.S.H.: Handheld imageless robotic total knee arthroplasty improves accuracy and early clinical outcomes when compared with navigation. Arthroplasty **7**(1) (Apr 2025). https://doi.org/10.1186/s42836-025-00303-4
18. Umeyama, S.: Least-squares estimation of transformation parameters between two point patterns. IEEE Transactions on Pattern Analysis and Machine Intelligence **13**(4), 376–380 (1991). https://doi.org/10.1109/34.88573
19. Wakelin, E.A., Tran, L., Twiggs, J.G., Theodore, W., Roe, J.P., Solomon, M.I., Fritsch, B.A., Miles, B.P.: Accurate determination of post-operative 3d component positioning in total knee arthroplasty: the aurora protocol. Journal of Orthopaedic Surgery and Research **13**(1) (Oct 2018). https://doi.org/10.1186/s13018-018-0957-0